




# Local variations in material and structural properties characterize murine thoracic aortic aneurysm mechanics

Matthew R. Bersi<sup>1,2</sup> · Chiara Bellini<sup>1,3</sup> · Jay D. Humphrey<sup>1</sup> · Stéphane Avril<sup>4</sup> 

Received: 5 May 2018 / Accepted: 14 September 2018 / Published online: 24 September 2018  
© Springer-Verlag GmbH Germany, part of Springer Nature 2018

## Abstract

We recently developed an approach to characterize local nonlinear, anisotropic mechanical properties of murine arteries by combining biaxial extension–distension testing, panoramic digital image correlation, and an inverse method based on the principle of virtual power. This experimental–computational approach was illustrated for the normal murine abdominal aorta assuming uniform wall thickness. Here, however, we extend our prior approach by adding an optical coherence tomography (OCT) imaging system that permits local reconstructions of wall thickness. This multimodality approach is then used to characterize spatial variations of material and structural properties in ascending thoracic aortic aneurysms (aTAA) from two genetically modified mouse models (fibrillin-1 and fibulin-4 deficient) and to compare them with those from angiotensin II-infused apolipoprotein E-deficient and wild-type control ascending aortas. Local values of stored elastic energy and biaxial material stiffness, computed from spatial distributions of the best fit material parameters, varied significantly with circumferential position (inner vs. outer curvature, ventral vs. dorsal sides) across genotypes and treatments. Importantly, these data reveal an inverse relationship between material stiffness and wall thickness that underlies a general linear relationship between stiffness and wall stress across aTAAs. OCT images also revealed sites of advanced medial degeneration, which were captured by the inverse material characterization. Quantification of histological data further provided high-resolution local correlations among multiple mechanical metrics and wall microstructure. This is the first time that such structural defects and local properties have been characterized mechanically, which can better inform computational models of aortopathy that seek to predict where dissection or rupture may initiate.

**Keywords** Inverse method · Constitutive relation · Material heterogeneity · Structure–function · Aortic aneurysm · Fibrillin-1 · Fibulin-4

---

**Electronic supplementary material** The online version of this article (<https://doi.org/10.1007/s10237-018-1077-9>) contains supplementary material, which is available to authorized users.

---

✉ Stéphane Avril  
avril@emse.fr

- <sup>1</sup> Department of Biomedical Engineering, Yale University, New Haven, CT, USA
- <sup>2</sup> Department of Biomedical Engineering, Vanderbilt University, Nashville, TN, USA
- <sup>3</sup> Department of Bioengineering, Northeastern University, Boston, MA, USA
- <sup>4</sup> INSERM U1059, SAINBIOSE, CIS-EMSE, Mines Saint-Etienne, University of Lyon, 42023 Saint Etienne, France

## 1 Introduction

Ascending aortic disease manifesting as aneurysm, dissection, or rupture is a major clinical concern (Jondeau and Boileau 2012). Dissection and rupture are, for example, cardiovascular events with high morbidity and mortality (Masuda et al. 1991). To better inform therapeutic decision making, there is a pressing need for an increased understanding of the mechanical properties that result from localized changes in wall composition and microstructure (Elefteriades 2008; Wu et al. 2013; de Wit et al. 2013; Tsamis et al. 2013). Unfortunately, such information is often difficult to obtain from human subjects given the need for longitudinal data to characterize the natural history of these conditions. Mouse models, in contrast, allow controlled longitudinal studies and detailed assessments of local wall mechanics and histology.

Common models of ascending thoracic aortic aneurysms (aTAAs) include mice with mutations to genes that encode the elastin-associated glycoproteins fibulin-4 (*Fbln4*<sup>SMKO</sup>) and fibrillin-1 (*Fbn1*<sup>mgR/mgR</sup>). Smooth muscle cells from *Fbln4*<sup>SMKO</sup> mice do not produce fibulin-4, resulting in marked elastic fiber disorganization (Huang et al. 2010), and *Fbn1*<sup>mgR/mgR</sup> mice produce only ~20% of normal fibrillin-1, resulting in a progressive fragmentation of the elastic fibers (Pereira et al. 1999). While *Fbln4*<sup>SMKO</sup> mice exhibit severe thoracic aneurysms, *Fbn1*<sup>mgR/mgR</sup> mice often have ascending aortic aneurysms with concurrent aortic root dilatation and reduced life expectancy due to aneurysmal rupture, consistent with a severe manifestation of Marfan syndrome (Cook et al. 2015). These two mouse models have been used extensively to study histopathological changes, and in some studies the associated macroscopic alterations to mechanical functionality and structural integrity (Marque et al. 2001; Huang et al. 2013; Schwill et al. 2013). Additionally, although it does not phenocopy human aortic disease, chronic angiotensin II infusion in apolipoprotein E-deficient mice (*ApoE*<sup>-/-</sup> + AngII) has also been shown to yield aTAAs (Rateri et al. 2014; Trachet et al. 2016). Notwithstanding the utility of traditional analyses of global wall properties in aTAAs, aortic dissection and rupture initiate locally. Hence, quantification of bulk material behaviors provides limited information on disease susceptibility. Correlations between local wall composition and material behavior are needed to understand better the mechanical state that renders a vessel susceptible to failure.

Toward this end, we recently developed an experimental–computational approach suitable for quantifying spatial variations in material and structural properties in murine arteries and potentially correlating these variations with the underlying microstructure (Bersi et al. 2016a). This imaging-based inverse characterization employs the principle of virtual power and can determine locally varying values of constitutive parameters from a set of full-field geometric data acquired during mechanical testing (Avril et al. 2010). By combining traditional biaxial testing (Ferruzzi et al. 2013) with a novel panoramic digital image correlation (pDIC) method (Genovese et al. 2013), we are able to obtain full-field strain measurements at multiple equilibrium configurations. The utility of this method was illustrated for suprarenal abdominal aortas excised from non-aneurysmal mice (Bersi et al. 2016a).

We previously invoked the common assumption of uniform wall thickness within select regions of the aorta (Bersi et al. 2016a), yet thickness can vary spatially in complex vascular lesions (Choudhury et al. 2009). Hence, we have now augmented our prior experimental–computational approach by adding optical coherence tomography (OCT) measurements that permit a full-field reconstruction of wall thickness. Using this new multimodality imaging approach (pDIC +

OCT), we characterized local variations in material and structural properties of aTAAs from two common genetically modified mouse models (*Fbln4*<sup>SMKO</sup> and *Fbn1*<sup>mgR/mgR</sup>) and compared them with results from angiotensin II-treated apolipoprotein E-deficient (*ApoE*<sup>-/-</sup> + AngII) and wild-type (WT) control mice. We found marked spatial variations in material and structural properties for the representative aTAAs, which correlated with local wall thickness and wall composition, as measured by quantitative histology. The results reveal that our multimodality approach can faithfully identify locations and properties of underlying defects in tissue microstructure that associate with severe thoracic aortopathies.

## 2 Materials and methods

### 2.1 Animal models

All animal protocols were approved by the Yale University Institutional Animal Care and Use Committee. Briefly, adult male mice were euthanized using an intraperitoneal injection of Beuthanasia-D and the ascending thoracic aorta—from the aortic root to the brachiocephalic artery—was excised en bloc. Samples were obtained from *Fbln4*<sup>SMKO</sup>, *Fbn1*<sup>mgR/mgR</sup>, and *ApoE*<sup>-/-</sup> + AngII mice with aneurysmal dilatations as well as from wild-type (WT) control mice.

### 2.2 Biomechanical testing

The ascending aorta was prepared for mechanical testing by removing excess perivascular tissue and ligating the left carotid artery, left subclavian artery, and distal aortic arch using single strands from braided 7-0 nylon suture. Each vessel was then subjected to a multi-step mechanical testing protocol. First, the two ends of the ascending aorta were secured to pulled glass cannulae using 6-0 sutures. The mounted specimen was then placed within a custom, computer-controlled biaxial testing system (Gleason et al. 2004) and subjected to standard loading protocols: cyclic pressurization from 0 to 140 mmHg at three fixed axial stretches (the in vivo value and  $\pm 5\%$  of this value) and cyclic axial extension at four fixed pressures (from 10 to 140 mmHg). All tests were performed in Hanks Buffered Salt Solution (HBSS) at  $\sim 37^\circ\text{C}$  following standard acclimation and preconditioning protocols (Ferruzzi et al. 2013). Further details on our methods of biaxial testing and data analysis are given elsewhere (Bellini et al. 2017; Bersi et al. 2017).

Next, specimens were re-cannulated using a custom blunt-ended double-needle composite using the same suture locations and oriented vertically within a custom pDIC system to monitor full-field surface deformations (Bersi et al.

2016a). Data were acquired at multiple combinations of pressure (every 10 mmHg from 0 to 140 mmHg) and axial stretch (the in vivo value and  $\pm 5\%$ , as identified during standard biaxial testing). Individually tracked surface points were used to reconstruct the overall surface geometry in each deformed configuration, which was rotated numerically to position the outer curvature of the aorta at  $0^\circ$ . All material points were then defined by circumferential (denoted  $\Theta_m$ ,  $1 \leq m \leq 40$ ) and axial (denoted  $Z_n$ ,  $1 \leq n \leq 25$ ) coordinate positions. A computationally convenient reference configuration was chosen at the in vivo value of axial stretch and 80 mmHg, which was defined by a regular surface mesh described in cylindrical coordinates by

$$R_{mn} = R_{\text{pDIC}}(\Theta_m, Z_n), \quad (1)$$

where  $R_{\text{pDIC}}$  denotes the point set defining the reconstructed pDIC surface. The displacement vector  $\mathbf{u}_{mn}(t)$  was calculated at each of these nodes from the neighboring full-field surface deformations, as measured by the pDIC system at each combination of pressure and axial stretch, which was parameterized by time  $t$  though achieved quasi-statically. Nodal displacements enabled a straightforward calculation of Green strain within each surface element at each time (Genovese 2009).

### 2.3 Optical coherence tomography

The re-cannulated vessels were also scanned with a commercially available optical coherence tomography (OCT) system (Thorlabs, Inc., NJ) to provide through-the-wall thickness information in a subset of deformation states (every 20 mmHg from 0 to 140 mmHg for the same three values of axial stretch). OCT is a noninvasive, non-contacting imaging modality that can achieve micron-resolution volumetric images in translucent, light scattering media such as biological soft tissues. Its penetration depth allows imaging through the wall of a murine artery. All OCT images were acquired using an index of refraction of  $n = 1.38$  (van der Meer et al. 2011).

Given the larger than normal diameter of the aTAA samples, volumetric images were acquired at four rotationally symmetric locations about the central axis of the vessel and 3D image registration was used to obtain full-field volumetric measurements. Specifically, prior to image registration, volumes were smoothed by median filtering to reduce local variations in intensity and were offset to increase overlap of regions shared by each image. Overlapping regions were automatically cropped, and an iterative 3D registration scheme, based on the Mattes mutual information metric, was used to identify an optimal rigid transformation between cropped volumes. To ensure congruent final volumes, individual volumes were resliced after each registration and

identified transformations were applied in a clockwise manner; this resulted in images with complete vessel cross sections at each slice. The multi-step, iterative, 3D image registration framework was built using image-merging libraries provided with the TubeTK extension in 3D Slicer (Aylward and Bullitt 2002; Fedorov et al. 2012).

Following image registration, inner and outer wall contours were segmented at each cross section of the reference OCT volume (i.e., at the in vivo axial stretch and 80 mmHg) using semiautomatic image thresholding. Co-registration between the reconstructed pDIC surface and outer OCT contour ensured a consistent mapping between full-field deformations and wall thickness. Thus, an optimal 3D rigid transformation between point sets, accounting for potential rotational and translational offsets, was identified using a single-value decomposition. After co-registration, outer wall OCT contour points  $R_{\text{OCT}}^o$  at the same circumferential and axial positions as those on the reconstructed pDIC surface mesh  $R_{mn}$  were identified and denoted  $R_{mn}^o = R_{\text{OCT}}^o(\Theta_m, Z_n)$ . At every outer wall nodal position  $R_{mn}^o$  in the reference configuration, local wall thickness  $H_{mn}$  was defined as the minimum distance to the inner wall contour on the same OCT cross section. Similarly, for each loading state at which OCT images were acquired (denoted by time  $t$ ), local distances between inner and outer wall contours were calculated at each node and denoted  $h_{mn}(t)$ . The distance  $h_{mn}(t)$  is not strictly the local thickness of the vessel as the cross-sectional plane may not necessarily cut normal to the vessel surface, particularly when the vessel is curved. When curvature is small, however,  $h_{mn}(t)$  is approximately the local wall thickness. Note that the OCT image quality was less at the ends of each sample due to cannulation; thus, wall thickness  $H_{mn}$  could often not be accurately reconstructed at these locations. To eliminate such edge effects, the upper and lower 10% of the sample was excluded from all analyses. For these and other points ( $m, n$ ) where thickness could not be estimated, a local average was assigned to generate a contiguous mesh for further data processing and analysis. Ultimately, however, no material property was identified at locations where the thickness was not measured reliably.

In addition to the OCT-based data, average values of the unloaded wall thickness were measured from transversely cut rings using a dissection microscope (Ferruzzi et al. 2013). These values were used to estimate the average wall thickness at the in vivo axial stretch and 80 mmHg, based on the assumption of a (locally) thick-walled incompressible cylinder. The computed values for each group were in good agreement (i.e.,  $\leq 10 \mu\text{m}$  difference) with OCT-measured values, consistent with the common assumption of isochoric motions.

## 2.4 Histology

Following the multi-step mechanical testing and imaging protocol, ascending aortic segments were fixed overnight in 10% neutral buffered formalin and stored in 70% ethanol. Samples were then embedded in paraffin, sectioned at 5  $\mu\text{m}$ , and stained with Movat's pentachrome (MOV) to visualize local wall constituents—elastic lamellae, collagen fibers, smooth muscle cells (SMCs), and glycosaminoglycans (GAGs). An Olympus BX/51 microscope (Olympus Inc., Center Valley, PA), equipped with an Olympus DP70 digital camera and 40X objective, was used to acquire high-resolution images of stained sections. Individual images were combined to form composite images of each cross section (Image Composite Editor, Microsoft Research), which were used for further analysis.

Images were analyzed using custom MATLAB software to measure average constituent area fractions and layer-specific wall percentages in each cross section. The average ratio of media thickness  $h_{\text{med}}$  to overall wall thickness  $h_{mn}$  was estimated from the measured wall percentages (Table 1). By combining these measurements, area fractions of the primary structural constituents (elastin  $\phi^e$ , smooth muscle  $\phi^m$ , and collagen  $\phi^c$ ) were quantified for both primary layers, media  $\phi_{\text{med}}$  and adventitia  $\phi_{\text{adv}}$  (Bersi et al. 2017). Average values of  $\phi_{\text{med}}^e$ ,  $\phi_{\text{adv}}^e$ ,  $\phi_{\text{med}}^m$ ,  $\phi_{\text{adv}}^m$ ,  $\phi_{\text{med}}^c$ , and  $\phi_{\text{adv}}^c$  are listed in Table 1 for each sample. Note that the GAG fraction was negligible ( $<3\%$  for each group) and was combined with the medial collagen fraction. Average area fractions were used in the inverse material characterization since histological measurements were within select cross sections, not over the entire computational domain. In addition, for comparison with local mechanical property measurements, histological images were divided into 40 circumferential partitions (cf. Fig. S7). Colorimetric analysis within each partition was used to estimate local area fractions (i.e., wall composition).

For comparison with OCT measurements, histological wall thickness was also estimated using an Eulerian solution to a pair of linear partial differential equations solved over the histological domain (Yezzi and Prince 2003). Briefly, following identification of inner and outer boundaries of the histological cross section, the normalized gradient of a harmonic function  $f$  between the two boundaries was used to define a unit tangent field. We obtained  $f$  by solving the Laplace equation  $\nabla^2 f = 0$  over the histological domain with Dirichlet boundary conditions of  $f = 0$  along the inner boundary and  $f = 1$  along the outer boundary. Using a fast marching algorithm, points on the inner boundary were then advected along the unit tangent field until reaching the outer boundary, and points on the outer boundary were advected along the negative unit tangent field until reaching the inner boundary in order to define correspondence trajec-

tories between the two boundaries. The local thickness field was given as the sum of these two Eulerian solutions over the histological domain; thickness was extracted at the midline between the inner and outer boundaries, as defined by one-half of the local correspondence trajectory distance (Rocha et al. 2007).

Correlations between histological and OCT measurements of wall thickness at each circumferential and axial position ( $m, n$ ) along the reconstructed surface were used to identify an optimal registration between modalities (cf. Fig. S6). To account for differences in wall thickness, as, for example, due to tissue shrinkage (histology) or biaxial loading (OCT), values were normalized prior to comparison. The maximum correlation coefficient was thus used to spatially orient (i.e., circumferential and axial position) each histological section in the overall reconstructed vessel geometry and thereby associate histological properties—such as circumferentially varying constituent area fractions and wall percentages—with identified material properties.

## 2.5 Inverse material characterization

A 3D structural mesh was constructed at the reference configuration (i.e., in vivo value of axial stretch and 80 mmHg) based on the geometry and thickness of co-registered pDIC and OCT datasets. Meshes consisted of 5000 brick elements (i.e., eight-node trilinear hexahedral elements with eight Gauss points). The mesh was structural in that edges of each hexahedron were aligned locally with material directions of the artery: radial, circumferential, and axial. As the geometry was not perfectly cylindrical, the axial direction was oriented parallel to the vessel axis, the radial direction was oriented perpendicular to the axial direction in the outward normal direction to the inner OCT contour at every cross section, and the circumferential direction was oriented perpendicular to the axial and radial directions. The outer surface mesh of the artery was derived from the pDIC surface reconstruction and consisted of  $40 \times 25$  nodes with cylindrical coordinates  $(R_{mn}, \Theta_m, Z_n)$ , as defined in Eq. 1. The interior nodes of the 3D mesh were defined by the coordinates  $(R_{mn} - \frac{q}{5}h_{mn}, \Theta_m, Z_n)$ , where  $1 \leq q \leq 5$ .

Components of the Green strain tensor were calculated for every combination of pressure and axial stretch using a finite element analysis. For this, components of the measured pDIC displacement vector  $\mathbf{u}_{mn}(t)$  were assigned to each outer surface node as a Dirichlet boundary condition. Similarly, intraluminal pressure was applied as a traction acting normal to each inner surface node. An incompressible neo-Hookean strain energy function was assigned, and the finite element model was solved at each Gauss point in FEBio (Maas et al. 2012). The resulting Green strains were then used to calculate the actual stress field using a more appropriate constitutive equation for the wall. Prior experience with

**Table 1** Average group- and layer-specific histological measurements of wall thickness ratios ( $h_{med}/h_{mn}$  and  $h_{adv}/h_{mn}$ ) and mass fractions for the elastin-dominated matrix ( $\phi^e$ ), smooth muscle and circumferential collagen ( $\phi^m$ ), diagonal collagen ( $\phi^d$ ), and axial collagen ( $\phi^a$ ) fibers

Group	Medial parameters					Adventitial parameters				
	$h_{med}/h_{mn}$	$\phi^e_{med}$	$\phi^m_{med}$	$\phi^d_{med}$	$\phi^a_{med}$	$h_{adv}/h_{mn}$	$\phi^e_{adv}$	$\phi^m_{adv}$	$\phi^d_{adv}$	$\phi^a_{adv}$
WT	0.69	0.59	0.38	0.015	0.015	0.31	0.01	0.04	0.83	0.12
<i>Fbln4<sup>SMKO</sup></i>	0.68	0.55	0.43	0.010	0.010	0.32	0.01	0.04	0.83	0.12
<i>Fbn1<sup>mgR/mgR</sup></i>	0.47	0.62	0.35	0.015	0.015	0.52	0.01	0.04	0.83	0.12
<i>ApoE<sup>-/-</sup> + AngII</i>	0.50	0.40	0.58	0.010	0.010	0.50	0.04	0.03	0.82	0.11

similar murine arteries revealed that a microstructurally motivated constrained mixture model describes the constitutive behavior well (Bellini et al. 2014). Thus, at each Gauss point  $k$ , we used a hyperelastic strain energy function  $W_k$ , defined per unit mass,

$$W_k(\xi) = \phi^e(\xi)W_k^e + \phi^m(\xi)W_k^m + \phi^d(\xi)W_k^d + \phi^a(\xi)W_k^a \quad (2)$$

where  $\xi \in [0, 1]$  denotes a through-the-thickness position between inner ( $\xi = 0$ ) and outer ( $\xi = 1$ ) radii,  $W_k^e$  is a neo-Hookean model describing the elastin-dominated matrix, and  $W_k^m$ ,  $W_k^d$  and  $W_k^a$  are coordinate invariant-based Fung-type exponential models that describe circumferential, diagonal, and axial contributions, respectively, of the fibrous tissue network dominated mainly by smooth muscle and collagen (Bersi et al. 2016a). The  $\phi^e$ ,  $\phi^m$ ,  $\phi^d$ , and  $\phi^a$  terms are related to the mass fractions of each constituent and defined based on their radial position  $\xi$ , such that

$$\phi^e(\xi) = \begin{cases} \phi^e_{med} & \text{if } \xi < \frac{h_{med}}{h_{mn}} \\ \phi^e_{adv} & \text{otherwise} \end{cases},$$

$$\phi^m(\xi) = \begin{cases} \phi^m_{med} + \beta^0_{med}\phi^c_{med} & \text{if } \xi < \frac{h_{med}}{h_{mn}} \\ \beta^0_{adv}\phi^c_{adv} & \text{otherwise} \end{cases},$$

$$\phi^d(\xi) = \begin{cases} \beta^\theta_{med}\phi^c_{med} & \text{if } \xi < \frac{h_{med}}{h_{mn}} \\ \beta^\theta_{adv}\phi^c_{adv} & \text{otherwise} \end{cases},$$

$$\phi^a(\xi) = \begin{cases} \beta^{90}_{med}\phi^c_{med} & \text{if } \xi < \frac{h_{med}}{h_{mn}} \\ \beta^{90}_{adv}\phi^c_{adv} & \text{otherwise} \end{cases}.$$

The constitutive relations used to describe the stored energy contribution from each constituent (cf., Eq. 2) were the same as in prior reports (Avril et al. 2010; Bersi et al. 2016a). Based on results from these prior studies, we prescribed the fractions of each fiber family to be  $[\beta^0_{med}, \beta^\theta_{med}, \beta^{90}_{med}] = [0.98, 0.01, 0.01]$  in the media, and  $[\beta^0_{adv}, \beta^\theta_{adv}, \beta^{90}_{adv}] = [0.04, 0.84, 0.12]$  in the adventitia. Note that  $\beta^0$ ,

$\beta^\theta$ , and  $\beta^{90}$  denote the fraction of circumferential, diagonal, and axial fibers, respectively.

Local values of material parameters were identified iteratively. Following initialization with an arbitrary set of material parameters assigned within a range of physiologically admissible values, the initial stress field was estimated. Next, a cost function, based on the principle of virtual power, was calculated as a measure of the deviation between the estimated and statically admissible stress fields (Avril et al. 2010). If the identified material parameters are not accurate, the updated stress field will not satisfy the equilibrium equations and will thus not be statically admissible. The cost function was minimized iteratively by updating the current set of material parameters using a combined optimization via a genetic algorithm and a nonnegative linear least-squares algorithm (Bersi et al. 2016a).

Following this local inverse material characterization (cf. Fig. S1 for mean  $R^2$  values), the final set of material parameters at each patch was used to compute the full-field distributions of stored energy, linearized circumferential material stiffness, and circumferential stress. Stored energy and material stiffness represent collective effects of the identified set of material parameters; values for each sample were computed at the in vivo axial stretch and pressure of either 80 mmHg for stored energy or 100 mmHg for material stiffness.

### 2.6 Statistics

All full-field metrics were divided into four regions around the vessel circumference—outer  $\in [-45^\circ, 45^\circ]$ , ventral  $\in [45^\circ, 135^\circ]$ , inner  $\in [135^\circ, -135^\circ]$ , and dorsal  $\in [-135^\circ, -45^\circ]$ —to facilitate statistical comparisons. Data throughout the manuscript are presented either as distributions (violin plots) or mean  $\pm$  standard deviation (SD) within each quadrant, unless otherwise noted. Differences between regions and genotypes were compared using two-way ANOVA followed by post hoc Tukey HSD tests for multiple comparisons. To avoid over-identification of significant differences given large sample sizes ( $n = 250$  per region), additional constraints were set based on the pair-

wise effect size, as measured by Hedges'  $g$ . Large effect sizes were defined as  $g > 1.3$ , where a value of 1.3 occurs when the mean of one group occurs in the 90<sup>th</sup> percentile of the second group. Thus, significance was defined for comparisons with  $p < 0.05$  and  $g > 1.3$ . Additionally, the two-way effect size  $\omega^2$  quantified how much of the observed variance in each metric was due to region or genotype. All effect sizes were calculated using the Measures of Effect Size Toolbox in MATLAB (Hentschke and Stüttgen 2011). Significant differences and effect sizes for all pairwise comparisons between regions and genotypes are summarized in lower diagonal matrices (Fig. S3). Correlations between histology and OCT thickness were assessed using the Pearson product-moment correlation coefficient,  $r$  (cf. Fig. S6).

### 3 Results

Representative samples from each of the four mouse models—wild type (*WT*), fibulin-4 deficient (*Fbln4<sup>SMKO</sup>*), fibrillin-1 deficient (*Fbn1<sup>mgR/mgR</sup>*), and angiotensin II-infused apolipoprotein E-deficient (*ApoE<sup>-/-</sup> + AngII*)—revealed marked differences in reconstructed ascending aortic geometries at sample-specific reference configurations (individual values of the in vivo axial stretch and a common pressure of 80 mmHg). The *Fbln4<sup>SMKO</sup>* specimen had the largest aneurysmal dilatation, followed by *Fbn1<sup>mgR/mgR</sup>* and *ApoE<sup>-/-</sup> + AngII*. The primary dilatation in the *Fbln4<sup>SMKO</sup>* sample was on the inner curvature of the mid-region of the ascending aorta, whereas the primary dilatation was on the outer curvature and closer to the aortic root for *Fbn1<sup>mgR/mgR</sup>* mice; *ApoE<sup>-/-</sup> + AngII* showed a diffuse increase in diameter, relative to *WT* (Fig. 1a).

Despite such differences in geometry, all specimens were amenable to full-field inverse material property identification with average values of  $R^2 > 0.78$  for each of the four groups (Fig. S1). Best fit values of four of the material parameters that reflect contributions of the primary structural constituents—elastin, SMC/circumferential collagen, diagonal collagen, and axial collagen—show distinct differences across groups (Fig. S2). Partitioning of vessels into outer, inner, ventral, and dorsal quadrants also revealed marked regional variations. *ApoE<sup>-/-</sup> + AngII* showed differences in the dorsal elastin parameter and ventral circumferential collagen parameter, compared to *WT* (Fig. S3A, B). *Fbln4<sup>SMKO</sup>* and *Fbn1<sup>mgR/mgR</sup>* typically had significantly higher parameter values than *WT* in most regions (Fig. S3A–D). Effects of such variations in material parameters can be collectively summarized into several materially relevant metrics, including stored energy and circumferential material stiffness.

First, regional distributions of elastic energy storage were computed at sample-specific values of in vivo axial stretch

and a common pressure of 80 mmHg and mapped onto their respective 3D geometry (Fig. 1a). To better visualize the full-field data, surfaces were also unwrapped to display values within each patch in an equivalent  $\theta - z$  plane (Fig. 1f–h). For comparison, the unwrapped *WT* energy distribution is given in Fig. S4A. Despite spatial variations in stored energy (Fig. 1b–e), there were no significant regional differences within *WT*, *Fbn1<sup>mgR/mgR</sup>*, or *ApoE<sup>-/-</sup> + AngII* specimens (e.g.,  $p > 0.05$  or  $g < 1.3$ ). In contrast, the *Fbln4<sup>SMKO</sup>* sample had significantly lower stored energy along the inner curvature than along the outer curvature, consistent with lower energy storage in the primary location of aneurysmal dilatation. Energy storage was greatest in the *WT* thoracic aorta, as expected, followed by *Fbn1<sup>mgR/mgR</sup>*, *Fbln4<sup>SMKO</sup>*, and *ApoE<sup>-/-</sup> + AngII*. This trend in energy storage is particularly evident when visualizing isoenergy contours (Fig. S5; cf. (Bersi et al. 2016b)). Despite higher average values in each region, *WT* energy storage was only significantly higher than *Fbn1<sup>mgR/mgR</sup>* in the outer quadrant and *Fbln4<sup>SMKO</sup>* in the outer and dorsal quadrants; *ApoE<sup>-/-</sup> + AngII* was significantly lower than all others in all regions (Fig. S3E). *Fbn1<sup>mgR/mgR</sup>* stored energy was significantly higher than *Fbln4<sup>SMKO</sup>* in all regions except along the outer curvature. That energy storage in the outer curvature is significantly reduced in all aneurysmal samples suggests that this might be a site of preferential remodeling associated with aTAAs.

Circumferential material stiffness was similarly computed at sample-specific values of in vivo axial stretch and a common pressure of 100 mmHg and then mapped onto 3D geometries as well as equivalent  $\theta - z$  planes (Fig. 2a, f–h). The unwrapped distribution of *WT* circumferential stiffness is in Fig. S4A. In contrast to stored energy, *Fbln4<sup>SMKO</sup>* and *Fbn1<sup>mgR/mgR</sup>* showed distinct locations of increased stiffness. That said, *Fbln4<sup>SMKO</sup>* and *Fbn1<sup>mgR/mgR</sup>* were not statistically different from one another in any region ( $p > 0.05$  in dorsal;  $g < 1.3$  in outer, ventral, and inner). Note that values of circumferential stiffness in *WT* and *ApoE<sup>-/-</sup> + AngII* were also not statistically different from each other in any region ( $p > 0.05$  in outer;  $g < 1.3$  in ventral, inner, and dorsal), but were yet significantly less than *Fbln4<sup>SMKO</sup>* and *Fbn1<sup>mgR/mgR</sup>* in all regions (Fig. 2b–e). Interestingly, while *WT* had significantly increased stiffness on the inner curvature relative to the outer curvature, *Fbln4<sup>SMKO</sup>* and *Fbn1<sup>mgR/mgR</sup>* each had higher stiffness on the outer curvature relative to the inner curvature; *ApoE<sup>-/-</sup> + AngII* showed no differences across regions (Fig. S3F). Regional distributions of circumferential stiffness again highlight the outer curvature as a location of adverse remodeling in *Fbln4<sup>SMKO</sup>* and *Fbn1<sup>mgR/mgR</sup>* aneurysmal samples. That aneurysmal dilatation associates with both reduced energy storage and an increased circumferential stiffness is consistent with findings based on traditional biaxial testing (Bellini et al. 2017).

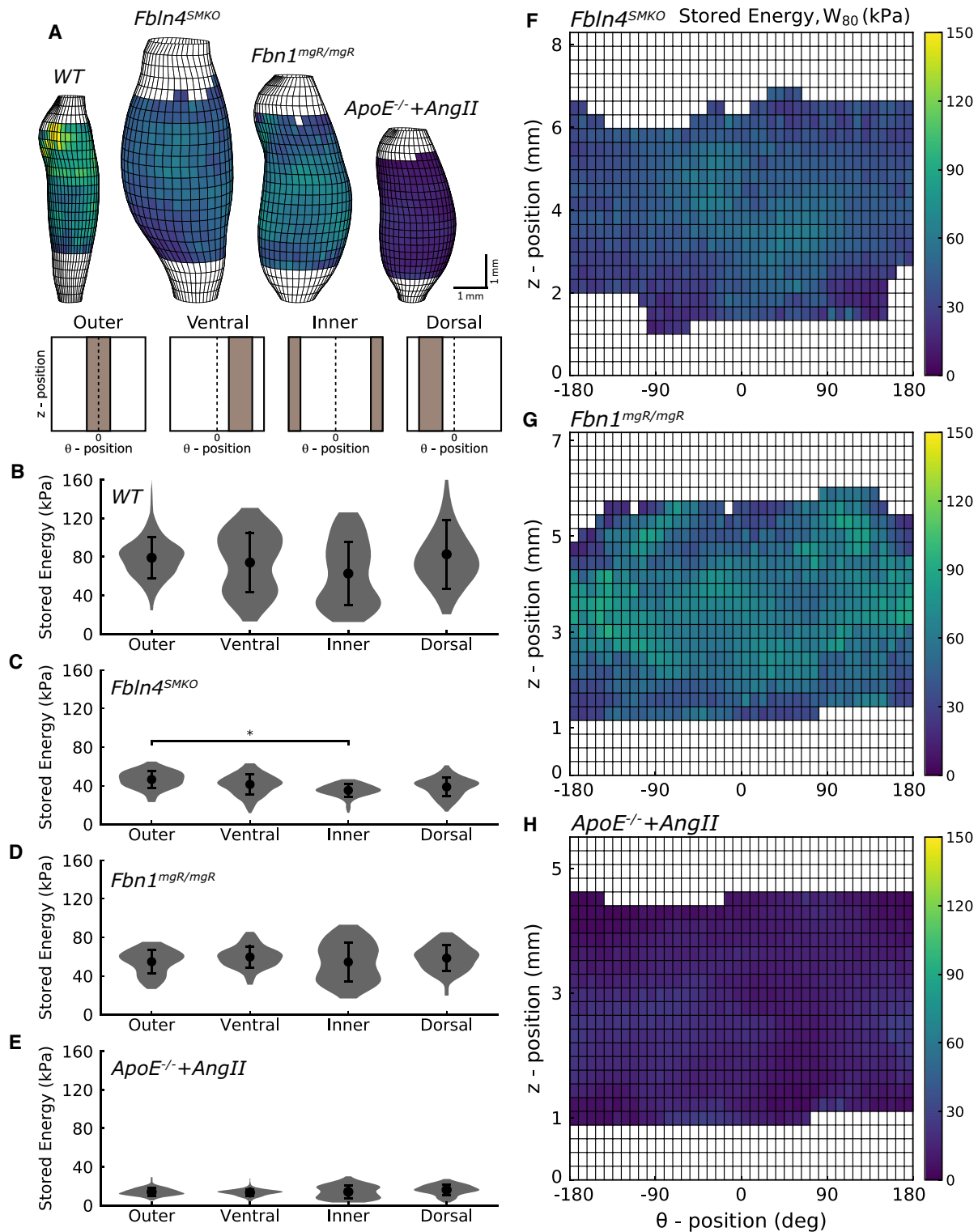


**Fig. 1** Spatial distributions of stored energy in thoracic aortic aneurysms. **a** Reconstructed reference configuration geometries with stored energy calculated point-wise at individual values of in vivo axial stretch and a common pressure of 80 mmHg. Values are compared across circumferential quadrants (**b–e**; defined in **a**) and parameterized  $\theta - z$  planes (**f–h**; *WT* in Fig. S4A). Regional distributions are shown as

violin plots with overlaid mean  $\pm$  standard deviation. Overbar denotes statistical significance between regions, where \* denotes  $p < 0.05$  and  $g > 1.3$ . For clarity, statistical differences between groups are not indicated; all pairwise comparisons and significant differences are indicated in Fig. S3E

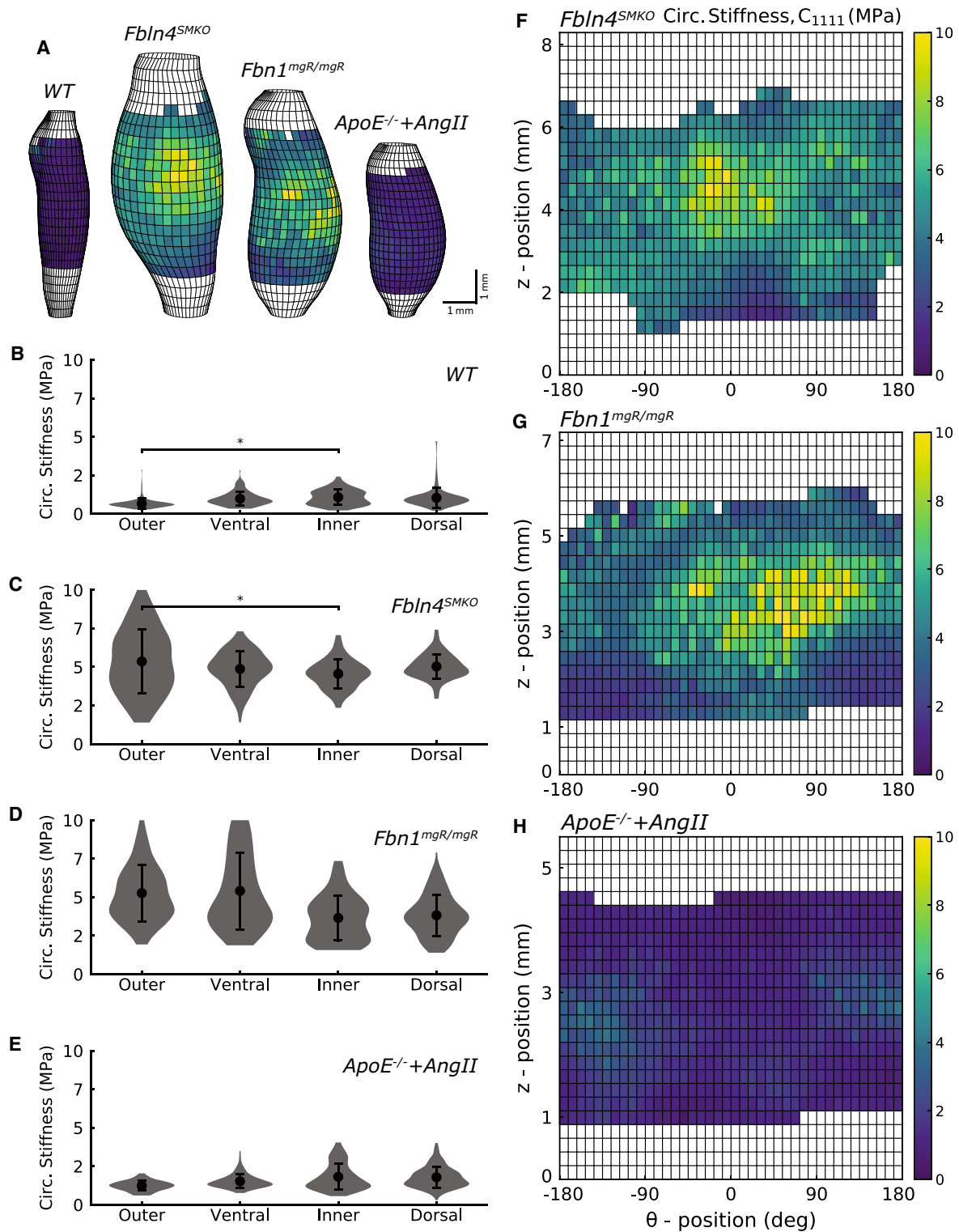


**Fig. 2** Spatial distributions of circumferential material stiffness in thoracic aortic aneurysms. **a** Reconstructed reference configuration geometries with circumferential stiffness calculated at individual in vivo axial stretches and 100 mmHg. Values are compared across circumferential quadrants (**b–e**; defined in Fig. 1a) or in a parameterized  $\theta - z$  plane (**f–h**; WT in Fig. S4A). Regional distributions are shown as violin

plots with overlaid mean  $\pm$  standard deviation. Overbar denotes statistical significance between regions, where \* denotes  $p < 0.05$  and  $g > 1.3$ . For clarity, statistical differences between groups are not indicated; all pairwise comparisons and significant differences are indicated in Fig. S3F



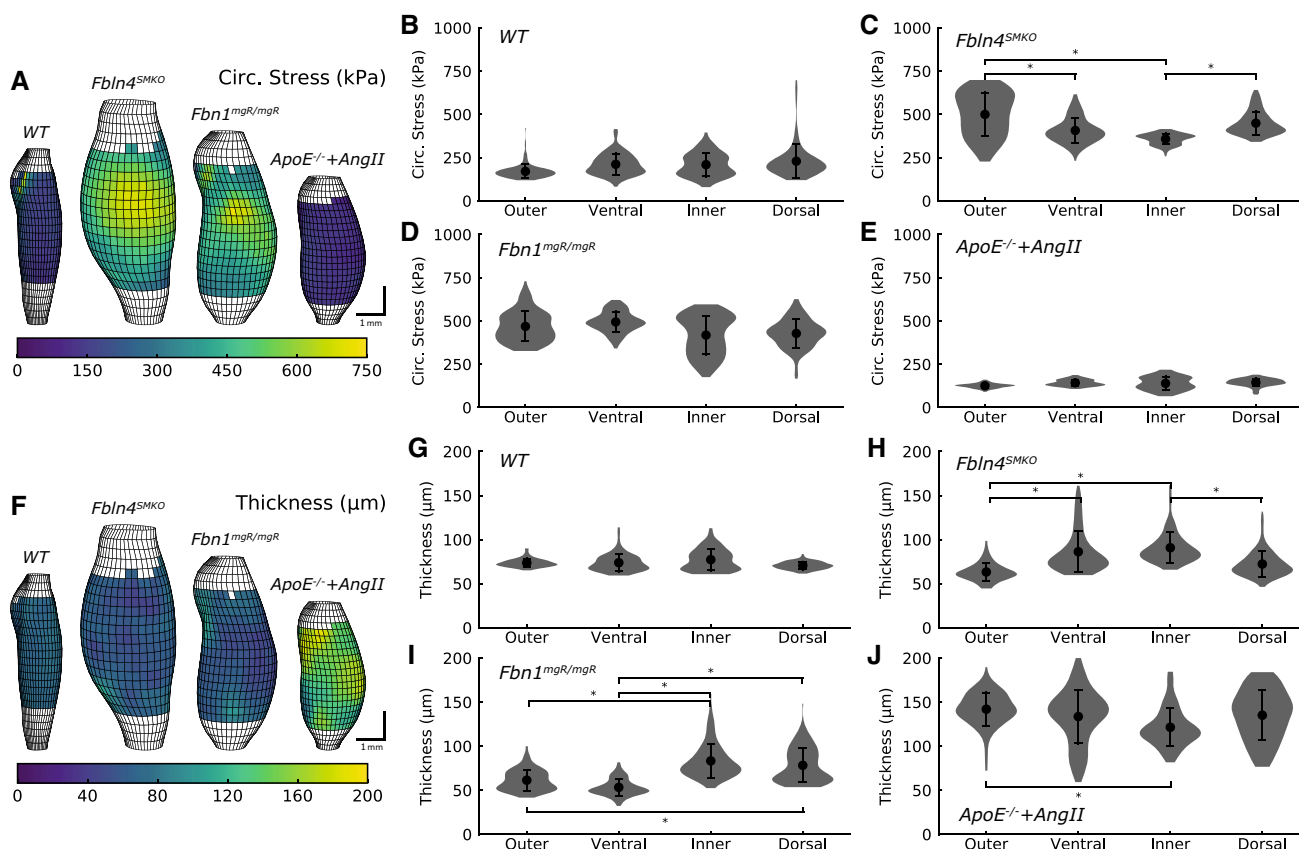


**Fig. 3** Spatial distributions of circumferential stress and wall thickness in thoracic aortic aneurysms. Reconstructed reference configuration geometries with either circumferential stress (**a**) or wall thickness (**f**) shown over the vessel surface. Circumferential stress is calculated at individual in vivo axial stretches and 100 mmHg, and values are compared across circumferential quadrants (**b–e**, **g–j**; parameterized  $\theta - z$

planes for each group are in Fig. S4B, C). Regional distributions are shown as violin plots with overlaid mean  $\pm$  standard deviation. Overbar denotes statistical significance between regions, where \* denotes  $p < 0.05$  and  $g > 1.3$ . For clarity, statistical differences between groups are not indicated; all pairwise comparisons and significant differences are indicated in Fig. S3G, H

Again using the identified material parameters (cf. Fig. S2), we next reconstructed the circumferential stress distribution for each sample to characterize regions of adaptive remodeling based on comparisons to local wall thickness. Circumferential stresses were computed at sample-specific in vivo axial stretches and a pressure of 100 mmHg (Fig. 3a–e) accounting for local variations in wall thickness measured by OCT (Fig. 3f–j); planar distributions for each group are shown in Fig. S4B–C. Similar to stored energy, we found no significant regional differences (e.g.,  $p > 0.05$  or  $g < 1.3$ ) among WT, *Fbn1<sup>mgR/mgR</sup>*, and *ApoE<sup>-/-</sup> + AngII* specimens. For *Fbln4<sup>SMKO</sup>*, a location of increased circumferential stress (Fig. 3a) resulted in statistically higher values in the outer curvature relative to the ventral and inner quadrants, with the inner curvature also having statistically lower values of stress than the dorsal quadrant (Fig. 3c). Although similar, *Fbn1<sup>mgR/mgR</sup>* and *Fbln4<sup>SMKO</sup>* had the highest overall stresses, consistent with a large increase in diameter with little increase in thickness, relative to WT (Fig. 3c, d, h, i). That said, *Fbn1<sup>mgR/mgR</sup>* had significantly higher stresses than *Fbln4<sup>SMKO</sup>* in the ventral and inner quadrants. WT had a

nearly uniform stress field that was significantly lower than both *Fbn1<sup>mgR/mgR</sup>* and *Fbln4<sup>SMKO</sup>* and significantly higher than *ApoE<sup>-/-</sup> + AngII* in all regions (Fig. S3G). Indeed, the hypertensive *ApoE<sup>-/-</sup> + AngII* model had the lowest stresses of all groups, consistent with the greatest increase in wall thickness.

Whereas the WT ascending aorta had a nearly uniform wall thickness, all aneurysmal samples exhibited spatial differences in thickness. In particular, *Fbn1<sup>mgR/mgR</sup>* and *Fbln4<sup>SMKO</sup>* had a significantly increased thickness on the inner curvature relative to the outer curvature. Moreover, for *Fbln4<sup>SMKO</sup>*, the inner curvature thickness was also significantly higher than the dorsal thickness, and the outer curvature thickness was significantly lower than the ventral thickness (Fig. 3h). For *Fbn1<sup>mgR/mgR</sup>*, the ventral thickness was significantly lower than both the inner and dorsal thickness, and the dorsal thickness was also significantly higher than the outer curvature thickness (Fig. 3i). Interestingly, due to several locations of medial damage, *ApoE<sup>-/-</sup> + AngII* exhibited the opposite variations, with higher thickness on the outer as opposed to inner curvature; it also

exhibited the greatest overall variation in thickness across regions (Fig. 3j). While  $ApoE^{-/-}$  + AngII had significantly greater thickness than all other groups in all regions, only the ventral  $Fbn1^{mgR/mgR}$  quadrant was significantly thinner than  $Fbn4^{SMKO}$  and  $WT$ . Most notably, wall thickness in the  $Fbn1^{mgR/mgR}$  and  $Fbn4^{SMKO}$  outer curvatures was significantly less than  $WT$  (Fig. S3H), consistent with the aforementioned findings of altered stored energy and material stiffness. Additionally, regions of increased circumferential stress in  $Fbn1^{mgR/mgR}$  and  $Fbn4^{SMKO}$  samples often occurred independent of regions of decreased wall thickness. This finding may suggest that regional distributions of material properties in  $Fbn4^{SMKO}$  and  $Fbn1^{mgR/mgR}$  aortas resulted more from maladaptive than adaptive growth and remodeling processes. Finally, although regional differences existed, the measured variance in each material, geometric, and structural metric, as measured by the two-way measure of effect size  $\omega^2$ , was better explained by differences between groups as opposed to differences across regions (Fig. S3).

To further investigate the relationship between the measured mechanical properties, wall thickness, and wall composition of aTAAs, we next developed a scheme to co-register histological and OCT cross sections. Using normalized wall thickness (Fig. S6A), an optimal registration was defined based on the maximum linear correlation coefficient obtained when comparing normalized histological thickness with normalized OCT thickness at all circumferential and axial positions across an entire sample. There was good agreement between normalized thicknesses for the aneurysmal samples ( $r \geq 0.72$ ), but less so for the  $WT$  sample ( $r = 0.55$ ) due to less circumferential variation in thickness. Normalized thickness profiles and linear correlations at the site of optimal registration for each specimen can be found in Fig. S6B. Registered histological images with representative comparisons between modalities (annotated by green boxes) are shown in Fig. 4a, d, g, j, for each specimen. Note that the histology–OCT registration captures areas of local thickening in  $Fbn4^{SMKO}$  (Fig. 4d) and medial degeneration in  $ApoE^{-/-}$  + AngII (Fig. 4j). Polar representations of wall thickness near the location of optimal registration (blue lines, insets; Fig. 4b, e, h, k) again reveal strong similarities between histology and OCT, particularly in the highlighted regions of comparison. Note that the green wedge corresponds to the green rectangle in Fig. 4a, d, g, j. In addition to wall thickness, registration further allowed local comparisons between microstructure and mechanical properties.

Circumferential variations in layer percentages and wall composition were computed based on a local partitioning of histological cross sections (Fig. S7). Consistent with minimal variations in thickness,  $WT$  had the least circumferential variation in medial percentage (Fig. 4c). Indeed, while  $WT$  and  $Fbn4^{SMKO}$  were not different, both  $Fbn1^{mgR/mgR}$  and  $ApoE^{-/-}$  + AngII had significantly higher adventitial

percentages, with the hypertensive  $ApoE^{-/-}$  + AngII value being significantly higher than in all other groups (Fig. 5d).  $Fbn4^{SMKO}$ ,  $Fbn1^{mgR/mgR}$ , and  $ApoE^{-/-}$  + AngII (Fig. 4f, i, l) each showed locations of increased adventitial percentage at  $45^\circ$ ,  $-135^\circ$ , or  $\pm 90^\circ$ , respectively. For  $Fbn4^{SMKO}$ , this co-localized with locally increased wall thickness; for  $Fbn1^{mgR/mgR}$  and  $ApoE^{-/-}$  + AngII, this co-localized with regions of advanced medial degeneration. Indeed, the media was often ulcerated in these regions and occupied  $< 35\%$  of the wall, a significant reduction from  $\sim 70\%$  in the healthy ascending aorta (cf. Fig. 4c). In general, all four groups tended to have higher medial percentages in the inner and outer quadrants compared to the dorsal and ventral quadrants, with highest values often on the inner curvature. Moreover, the total adventitial percentage increased in all aneurysmal samples. While the increase in  $Fbn4^{SMKO}$  and  $Fbn1^{mgR/mgR}$  was likely a consequence of medial reduction due to mutations in elastin-associated glycoproteins, the excessive adventitial thickening and collagen deposition in  $ApoE^{-/-}$  + AngII were likely a direct result of AngII-induced hypertension (Bersi et al. 2016b).

Comparison between the spatial trends in circumferential material stiffness (Fig. 2) and wall thickness (Fig. 3f–j) revealed an inverse relationship in aneurysmal samples. Indeed, by combining values from all three groups ( $Fbn4^{SMKO}$ ,  $Fbn1^{mgR/mgR}$ , and  $ApoE^{-/-}$  + AngII), we found that circumferential stiffness and thickness were related by a hyperbolic fit (red line; Fig. 5a). This relationship was not observed for  $WT$  (black line; Fig. 5a). Albeit not shown, similar trends were found between axial material stiffness and thickness in aneurysmal and  $WT$  samples. Because there is a linear relationship between stiffness and stress in materials having an exponential behavior (Fung 1967), and mean circumferential stress is inversely proportional to wall thickness, we also plotted the local relationship between circumferential stiffness and circumferential stress. Note that local and global circumferential stress–stretch responses agreed well for all samples (Fig. S8). As expected, linear relationships were identified between stiffness and stress, though with markedly different slopes for aneurysmal (red line) and  $WT$  (black line) samples (Fig. 5b). In particular, comparisons of the individual linear relations revealed a 2.2-fold, 3.7-fold, and 4.3-fold increase in slope for  $Fbn4^{SMKO}$ ,  $Fbn1^{mgR/mgR}$ , and  $ApoE^{-/-}$  + AngII, respectively, relative to  $WT$  (Fig. 5c). Recalling the measured differences in wall composition (cf. Fig. 4c, f, i, l), there was an exponential relationship between the stiffness–stress slope and adventitial percentage (Fig. 5d), consistent with a collagen-dominated material response associated with increased adventitia. Importantly, the local stiffness–stress response for each group revealed that aneurysmal samples also had greater dispersion about the theoretical linear relationship than  $WT$  (Fig. S9).

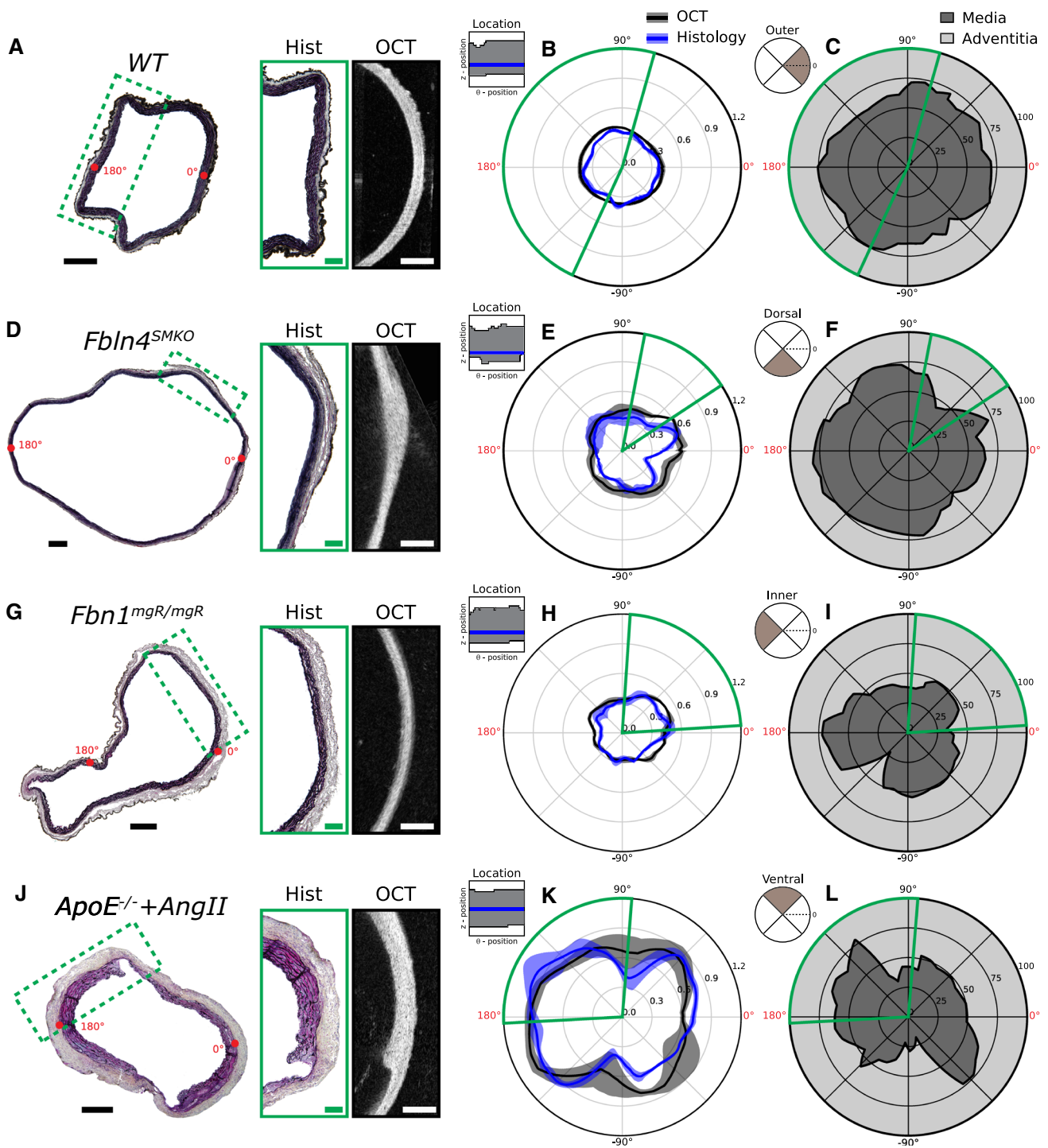


**Fig. 4** Registration between histology and OCT. Histological images show similar wall thickness trends as OCT images (green boxes; a, d, g, j). Following a linear correlation analysis (cf. Fig. S6), there is good agreement between normalized histology (blue curves) and OCT (black curves) wall thicknesses, particularly at the location of optimal registration (blue line, inset; b, e, h, k). Quantification of histological

images (*n* = 3-5 per group) revealed average circumferential variations in layer percentages (dark/light gray; c, f, i, l). Annotations of 0° and 180° (red text; a, d, g, j) correspond to specific locations (i.e., outer curvature at 0°) in the polar plots. Circumferential quadrants are shown schematically (insets; c, f, i, l). Scale bars = 100 μm (black) or 50 μm (green/white)

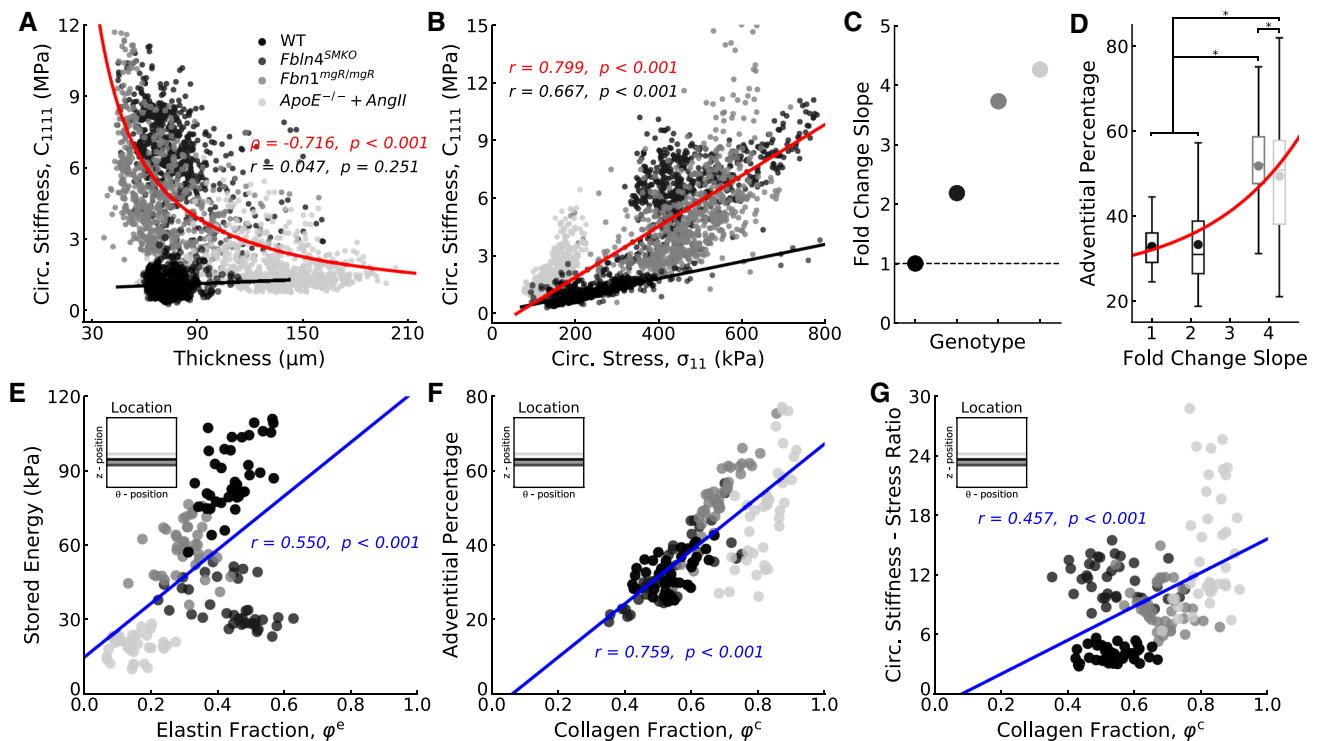


**Fig. 5** Trends in local behavior across thoracic aortic aneurysms. **a** Comparisons between circumferential material stiffness and wall thickness revealed a hyperbolic relationship in aneurysmal samples (red curve) that was not observed in *WT* samples (black curve) and underlies **(b)** a linear relationship between stiffness and stress. Note the marked differences in slope between aneurysmal (red curve) and *WT* samples (black curve). **c** The slopes of the individual stiffness–stress responses increased in all aneurysmal samples relative to *WT*. **d** Comparison with adventitial percentage revealed an exponential relationship (red curve).

Using the dispersion in the stiffness–stress response, we derived a multivariate ellipse based on eigenvalues of the covariance matrix. Plotting concentric ellipses for up to five standard deviations about the multivariate mean vector revealed that all samples had measurable deviation from the mean, albeit to varying degrees (Fig. S9A–D). While all groups had  $\sim 90\%$  of the data within two standard deviations from the mean (e.g., 93, 85, 87, and 87% for *WT*,  $Fbln4^{SMKO}$ ,  $Fbn1^{mgR/mgR}$ , and  $ApoE^{-/-} + AngII$ , respectively), all aneurysmal samples had a smaller percentage of data within one standard deviation. Namely, *WT* had 64% of patches, whereas  $Fbln4^{SMKO}$ ,  $Fbn1^{mgR/mgR}$ , and  $ApoE^{-/-} + AngII$  had 38%, 49%, and 46%, respectively. This reduction in the percentage of data within one standard deviation quantitatively highlights the increased non-homogeneity in properties in aneurysmal samples (Fig. S9E–H). Additionally, this dispersion may suggest sub-optimal spatial mechano-adaptations in aneurysmal vessels and further reflects the marked spatial distributions of wall properties (Figs. 1, 2), geometry, and stress (Fig. 3).

Mean values of adventitial percentage are shown as markers above each box plot. Local histological analyses (cf. Fig. S7) further revealed positive correlations (blue curves) between **e** stored energy and elastin area fraction, **f** adventitial percentage and collagen area fraction, and **g** stiffness–stress ratio, an estimate of the local stiffness–stress slope, and collagen area fraction, at the location of optimal registration (insets; **e–g**). Overbar denotes statistical significance between groups, where \* denotes  $p < 0.05$  and  $g > 1.3$

Finally, circumferential variations in wall composition, based on a local partitioning (Fig. S7) and colorimetric analysis of histological images, were compared against local mechanical properties. At the locations of histological registration, all aneurysmal samples had lower elastin and higher collagen area fractions than *WT*. In particular,  $ApoE^{-/-} + AngII$  had the highest collagen fraction and lowest elastin fraction of all tested samples (Fig. 5e, f). Co-localization of mechanical properties and wall composition revealed a positive correlation between local stored energy and elastin ( $r = 0.550$ ; Fig. 5e). In general, this is to be expected as elastin is primarily responsible for endowing arteries with their resilience, that is, elasticity. That said, it is interesting that this trend is maintained across aneurysmal samples with varying degrees of elastin fragmentation (Bellini et al. 2017). Conversely, albeit not shown, we also found a negative correlation between local stored energy and collagen. Although there was increased collagen in the media of all aneurysmal samples, the adventitia was the primary location of collagen deposition, as shown by the strong positive correlation between local adventitial percentage and collagen ( $r = 0.759$ ;

Fig. 5f). Analogous to the stiffness–stress slope (Fig. 5b, c), we computed a local circumferential stiffness–stress ratio and observed a positive correlation with collagen ( $r = 0.457$ ; Fig. 5g). This suggests that collagen deposition modulates the intrinsic stiffness of the wall (not just strength) and thereby contributes to the increased stiffness in aneurysmal samples. Indeed, locations with the highest collagen content co-localized with predominant regions of medial ulceration (around  $\pm 90^\circ$ ) in the  $ApoE^{-/-}$  + AngII sample.

## 4 Discussion

Progressive aneurysmal enlargement of the ascending aorta is thought to increase the likelihood of an acute dissection or rupture due to the associated changes in matrix composition (Gomez et al. 2009) and persistent action of pulsatile hemodynamic loads (Bürk et al. 2012). To understand better the relationships between local wall microstructure and mechanics in the context of ascending aortic aneurysms, we identified local material properties in two genetically modified mouse models ( $Fbln4^{SMKO}$  and  $Fbn1^{mgR/mgR}$ ) and one pharmacologically induced model ( $ApoE^{-/-}$  + AngII) and compared results with those for a wild-type control ( $WT$ ). Using a quantitative registration between histological and OCT cross sections, we combined regional variations in wall composition and material properties to quantify, for the first time, local structure–function relationships in aTAAs. This approach highlighted regions of local thickening versus advanced medial degeneration that could be particularly vulnerable to dissection or rupture.

A primary function of the proximal aorta is to store elastic energy during systole and to use this energy to work on the blood during diastole (Faury 2001; Ferruzzi et al. 2015). One of the most dramatic differences between  $WT$  and all aneurysmal samples was the marked loss of energy storage capability in the latter (Figs. 1, S5). Loss of energy storage indicates a compromised mechanical functionality and typically results from one of two changes (Bersi et al. 2016b): loss of elastic fiber integrity, which reduces the ability of these fibers to store energy, or increased fibrillar collagen deposition, which prevents the wall from distending and thereby limits the deformation of competent elastic fibers. Herein, stored energy (Fig. 1) correlated with both the elastin material parameter  $c^e$  (Fig. S2) and elastin area fraction  $\varphi^e$  (Fig. 5e) in  $Fbln4^{SMKO}$  and  $Fbn1^{mgR/mgR}$ , and to a lesser extent in  $ApoE^{-/-}$  + AngII. Interestingly,  $Fbln4^{SMKO}$  had the largest diameter and also showed the greatest spatial variation in stored energy, with the most dramatic reduction on the inner curvature, the primary site of aneurysmal dilatation. Since functional elastic fibers cannot be produced or repaired by intramural cells in maturity, progressive aneurysmal growth leads to increased fragmentation, loss of structural integrity,

and reduced energy storage capacity (Wilson and Humphrey 2014). On the other hand, while the collagen area fraction  $\varphi^c$  (Fig. 5f) was increased in all aTAA samples,  $ApoE^{-/-}$  + AngII had the most pronounced adventitial deposition of collagen. This suggests that both compromised elastic fiber integrity and excessive collagen deposition contribute to the loss of energy storage in these models of aTAA, albeit differently for different models. In particular, compromised elastic fibers likely dictate the loss of energy storage in  $Fbln4^{SMKO}$  and  $Fbn1^{mgR/mgR}$ , whereas hypertensive wall thickening and collagen deposition limit distension of otherwise-competent elastic fibers in  $ApoE^{-/-}$  + AngII. Indeed, a recent study of human aneurysmal tissue samples showed greater energy loss with increased collagen percentage in tricuspid aortic valve (TAV) patients (Shahmansouri et al. 2016a). Finally,  $WT$  and  $ApoE^{-/-}$  + AngII had similar material parameter values (Fig. S2), further suggesting that it was the structural differences (i.e., wall thickness) between groups that led to differences in mechanical response.

Importantly, intrinsic circumferential material stiffness was significantly higher than  $WT$  in both  $Fbln4^{SMKO}$  and  $Fbn1^{mgR/mgR}$ , but not  $ApoE^{-/-}$  + AngII, aTAAs (Fig. 2). This increase in stiffness is consistent with a progressive loss of elastic fibers and associated loss of undulation in the collagen fibers (Ferruzzi et al. 2011). It is also consistent with recent findings for murine and human aTAAs, showing that aneurysmal specimens have significant increases in bulk circumferential material and structural stiffness (Bellini et al. 2017) and that high circumferential stiffness is correlated with a reduced ultimate stretch of the tissue (Duprey et al. 2016). Indeed, the reduced expression of fibulin-4 or fibrillin-1 that leads to an increase in stiffness may also implicate a change in mechanosensing, which could further exacerbate the aneurysmal phenotype (Humphrey et al. 2015). Note that prior measurements in murine aTAAs were based on traditional biaxial mechanical testing (Bellini et al. 2017). Although pDIC testing measures local variations in material properties, we observed good agreement with global measurements from biaxial extension–inflation testing (Fig. S8).

The current study further shows that although stiffness is increased throughout the ascending thoracic aorta in aneurysm models with elastic fiber mutations, local changes tended to occur where the underlying microstructure experienced marked degeneration. In particular, we observed a hyperbolic relationship between stiffness and thickness across all aneurysmal samples (Fig. 5a) and found that the lowest values of the circumferential stiffness–stress ratio, an approximation of the local stiffness–stress slope, occurred in regions of advanced ulceration in  $ApoE^{-/-}$  + AngII samples (Fig. 5g). Although our constitutive framework makes no distinction between regions of ulcerated and non-ulcerated tissue, our method nonetheless identified regions of medial

degeneration in both *Fbn1<sup>mgR/mgR</sup>* and *ApoE<sup>-/-</sup>* + AngII samples (Fig. 4i, l). Future work focused on the material properties of tissue surrounding ulcerated regions will be of particular interest as we seek to understand better the mechanical consequences of local variations in properties and inform computational biomechanical models of aTAAs. Nonetheless, alterations to local circumferential material stiffness may also be an indicator of susceptibility to dissection or rupture. Such changes in material stiffness need not be monotonic, with marked increases (due to elastin degradation and collagen remodeling) possibly followed by decreases (due to collagen degradation or damage) that could precede failure. For example, human aTAA samples with high physiologic stiffness had reduced values of rupture stress suggesting a relationship between stiffness and disease susceptibility (Duprey et al. 2016). Given the likely progressive increase in stiffness, any acute increase in blood pressure could also significantly increase wall stress acutely and render aneurysmal vessels more susceptible to failure. Indeed, patients with aTAA, such as those with Marfan syndrome, should avoid strenuous activities that increase blood pressure acutely, such as weight lifting (Hatzaras et al. 2007; Martin et al. 2013).

Our findings also highlight the outer curvature as a region of adverse remodeling. Interestingly, it is often the outer curvature that experiences the largest dilatation in patients with aTAA (Gomez et al. 2009). We found correlations between regions of increased circumferential stiffness and decreased wall thickness, with the most pronounced regional differences between the inner and outer curvatures (Figs. 2, 3f–j, 5a). Similar regional variations in thickness and stiffness have been reported for human ascending aortas (Choudhury et al. 2009), namely that the medial quadrant (inner curvature) was significantly thicker than the lateral quadrant (outer curvature), though the difference was less significant for aTAAs (Shahmansouri et al. 2016b). Spatial variations in stiffness were also opposite those in thickness, with the thickest quadrant (inner curvature) being the most compliant and the thinnest quadrants (outer curvature and posterior) the stiffest. A possible explanation for this observation could be that the inner curvature of the ascending aorta contacts the pulmonary artery. Thus, although the wall is thicker, the added perivascular support may help to unload the inner curvature and reduce the need for increased material stiffness to withstand normal systolic blood pressures (Choudhury et al. 2009). Conversely, the outer curvature must compensate for this unloading and, upon excision and removal of perivascular support, results in the observed trends in stiffness and thickness on the inner and outer curvatures. Indeed, in vivo measurements reveal a more uniform stiffness distribution around the circumference of aTAAs (Alreshidan et al. 2017). Additionally, the majority of the wall stress is carried by the media under physiologic loads (Bellini et al. 2014), but in cases of increased pressure or aneurysmal dilation, the

adventitia can bear more of the overall load which should contribute to the increased stiffness. Indeed, we measured higher adventitial percentages on the outer versus inner curvature in all aneurysmal samples (cf. Fig. 4f, i, l).

Although the current study focused on results from a representative sample from each model of aTAA, the global mechanical properties of each tested sample are consistent with the average properties of each group (Bellini et al. 2017). We note that the principle of virtual power had difficulty converging over the full domain of several additional samples per group. Interestingly, these samples were ~25% shorter and had larger curvatures over the vessel surface in addition to length-to-diameter ratios of 2.4–3, which may not have been sufficient to avoid Saint–Venant effects (Bersi et al. 2016a). When performing such mechanical tests, it seems important, therefore, to maintain a length-to-diameter ratio  $\geq 5$ , which can become increasingly difficult with large aneurysms in the ascending aorta of the mouse. Nonetheless, these representative samples revealed multiple relationships between local mechanics and wall microstructure. Indeed, the different aTAA models, and spatial variations therein, collectively generated both global trends (across aneurysmal samples) relating material stiffness, stress, and thickness and local trends (within each aneurysm) relating wall composition and measured wall properties. There is, however, a need for caution when interpreting local changes from normal and a need for more detailed identification of local structure–function relationships in longitudinal studies of aneurysmal development. Of course, there is an inherent challenge to correlating mechanical changes with failure potential since samples must be harvested prior to in vivo failure without knowledge of whether or not a particular specimen would have progressively remodeled or ruptured. Toward this end, it can be useful to perform material characterizations at progressively higher in vitro loads with the hope that some vessels will fail during testing. Indeed, recent findings in a separate mouse model—containing a disruption of transforming growth factor beta receptor II (TGFBR2), which leads to increased structural vulnerability—show that some vessel failures can fortuitously be observed in vitro (Ferruzzi et al. 2016).

## 5 Conclusion

Full-field characterization of geometric, material, and structural properties in multiple mouse models of thoracic aortopathy reveals marked local and regional differences in elastic energy storage, material stiffness, wall thickness, and wall stress, with variations along both the length of the lesion and around its circumference (inner vs. outer curvature, and ventral vs. dorsal sides). Interestingly, the outer curvature of non-hypertensive aTAAs had both a lower wall thickness and a greater circumferential stiffness, consistent with the loca-

tion of maximal growth. It may be that when unable to control material stiffness, cells can still attempt to maintain structural stiffness. Yet, regions of highly advanced medial degeneration revealed an inability to increase structural stiffness (and presumably strength), which could potentially initiate dissection or rupture. These results highlight the need to understand better the local mechanobiological processes governing the balance between extracellular matrix production and degradation in health and disease, for it is ultimately alterations to this homeostatic balance that render vessels susceptible to vascular disorders.

**Acknowledgments** This work was supported by NIH grants R01 HL105297, R21 HL107768, and U01 HL116323 (to JDH), P01 HL134605 (to D. Rifkin), and ERC Grant ERC-2014-CoG BIOLOCHANICS (to SA).

## References

- Alreshidan M, Shahmansouri N, Chung J et al (2017) Obtaining the biomechanical behavior of ascending aortic aneurysm via the use of novel speckle tracking echocardiography. *J Thorac Cardiovasc Surg* 153:781–788. <https://doi.org/10.1016/j.jtcvs.2016.11.056>
- Avril S, Badel P, Duprey A (2010) Anisotropic and hyperelastic identification of in vitro human arteries from full-field optical measurements. *J Biomech* 43:2978–2985. <https://doi.org/10.1016/j.jbiomech.2010.07.004>
- Aylward SR, Bullitt E (2002) Initialization, noise, singularities, and scale in height ridge traversal for tubular object centerline extraction. *IEEE Trans Med Imaging* 21:61–75. <https://doi.org/10.1109/42.993126>
- Bellini C, Ferruzzi J, Roccabianca S et al (2014) A microstructurally motivated model of arterial wall mechanics with mechanobiological implications. *Ann Biomed Eng* 42:488–502. <https://doi.org/10.1007/s10439-013-0928-x>
- Bellini C, Bersi MR, Caulk AW et al (2017) Comparison of 10 murine models reveals a distinct biomechanical phenotype in thoracic aortic aneurysms. *J R Soc Interface* 14:20161036. <https://doi.org/10.1098/rsif.2016.1036>
- Bersi MR, Bellini C, Di Achille P et al (2016a) Novel methodology for characterizing regional variations in material properties of murine aortas. *J Biomech Eng* 138:1–15. <https://doi.org/10.1115/1.4033674>
- Bersi MR, Bellini C, Wu J et al (2016b) Excessive adventitial remodeling leads to early aortic maladaptation in angiotensin-induced hypertension. *Hypertension* 67:890–896. <https://doi.org/10.1161/HYPERTENSIONAHA.115.06262>
- Bersi MR, Khosravi R, Wujciak AJ et al (2017) Differential cell-matrix mechanoadaptations and inflammation drive regional propensities to aortic fibrosis, aneurysm or dissection in hypertension. *J R Soc Interface* 14:1–31. <https://doi.org/10.1098/rsif.2017.0327>
- Bürk J, Blanke P, Stankovic Z et al (2012) Evaluation of 3D blood flow patterns and wall shear stress in the normal and dilated thoracic aorta using flow-sensitive 4D CMR. *J Cardiovasc Magn Reson* 14:1–11. <https://doi.org/10.1186/1532-429X-14-84>
- Choudhury N, Bouchot O, Rouleau L et al (2009) Local mechanical and structural properties of healthy and diseased human ascending aorta tissue. *Cardiovasc Pathol* 18:83–91. <https://doi.org/10.1016/j.carpath.2008.01.001>
- Cook JR, Clayton NP, Carta L et al (2015) Dimorphic effects of transforming growth factor- $\beta$  signaling during aortic aneurysm progression in mice suggest a combinatorial therapy for Marfan syndrome. *Arterioscler Thromb Vasc Biol*. <https://doi.org/10.1161/ATVBAHA.114.305150>
- de Wit A, Vis K, Jeremy RW (2013) Aortic stiffness in heritable aortopathies: relationship to aneurysm growth rate. *Heart Lung Circ* 22:3–11. <https://doi.org/10.1016/j.hlc.2012.08.049>
- Duprey A, Trabelsi O, Vola M et al (2016) Biaxial rupture properties of ascending thoracic aortic aneurysms. *Acta Biomater* 42:273–285. <https://doi.org/10.1016/j.actbio.2016.06.028>
- Elefteriades JA (2008) Thoracic aortic aneurysm: reading the enemy's playbook. *Curr Probl Cardiol* 33:203–277. <https://doi.org/10.1016/j.cpcardiol.2008.01.004>
- Faury G (2001) Function-structure relationship of elastic arteries in evolution: From microfibrils to elastin and elastic fibres. *Pathol Biol* 49:310–325. [https://doi.org/10.1016/S0369-8114\(01\)00147-X](https://doi.org/10.1016/S0369-8114(01)00147-X)
- Fedorov A, Beichel R, Kalpathy-Cramer J et al (2012) 3D slicer as an image computing platform for the quantitative imaging network. *Magn Reson Imaging* 30:1323–1341. <https://doi.org/10.1016/j.mri.2012.05.001>
- Ferruzzi J, Collins MJ, Yeh AT, Humphrey JD (2011) Mechanical assessment of elastin integrity in fibrillin-1-deficient carotid arteries: implications for Marfan syndrome. *Cardiovasc Res* 92:287–295. <https://doi.org/10.1093/cvr/cvr195>
- Ferruzzi J, Bersi MR, Humphrey JD (2013) Biomechanical phenotyping of central arteries in health and disease: advantages of and methods for murine models. *Ann Biomed Eng* 41:1311–1330. <https://doi.org/10.1007/s10439-013-0799-1>
- Ferruzzi J, Bersi MR, Uman S et al (2015) Decreased elastic energy storage, not increased material stiffness, characterizes central artery dysfunction in fibulin-5 deficiency independent of sex. *J Biomech Eng* 137:31007. <https://doi.org/10.1115/1.4029431>
- Ferruzzi J, Murtada SI, Li G et al (2016) Pharmacologically improved contractility protects against aortic dissection in mice with disrupted transforming growth factor-beta signaling despite compromised extracellular matrix properties. *Arterioscler Thromb Vasc Biol* 36:919–927. <https://doi.org/10.1161/ATVBAHA.116.307436>
- Fung YC (1967) Elasticity of soft tissues in simple elongation. *Am J Physiol* 213:1532–1544
- Genovese K (2009) A video-optical system for time-resolved whole-body measurement on vascular segments. *Opt Lasers Eng* 47:995–1008. <https://doi.org/10.1016/j.optlaseng.2009.04.017>
- Genovese K, Lee Y-U, Lee AY, Humphrey JD (2013) An improved panoramic digital image correlation method for vascular strain analysis and material characterization. *J Mech Behav Biomed Mater* 27:132–142. <https://doi.org/10.1016/j.jmbbm.2012.11.015>
- Gleason RL, Gray SP, Wilson E, Humphrey JD (2004) A multi-axial computer-controlled organ culture and biomechanical device for mouse carotid arteries. *J Biomech Eng* 126:787. <https://doi.org/10.1115/1.1824130>
- Gomez D, Al Haj Zen A, Borges LF et al (2009) Syndromic and non-syndromic aneurysms of the human ascending aorta share activation of the Smad2 pathway. *J Pathol* 218:131–142. <https://doi.org/10.1002/path.2516>
- Hatzaras I, Tranquilli M, Coady M et al (2007) Weight lifting and aortic dissection: more evidence for a connection. *Cardiology* 107:103–106. <https://doi.org/10.1159/000094530>
- Hentschke H, Stüttgen MC (2011) Computation of measures of effect size for neuroscience data sets. *Eur J Neurosci* 34:1887–1894. <https://doi.org/10.1111/j.1460-9568.2011.07902.x>
- Huang J, Davis EC, Chapman SL et al (2010) Fibulin-4 deficiency results in ascending aortic aneurysms: a potential link between abnormal smooth muscle cell phenotype and aneurysm progression. *Circ Res* 106:583–592. <https://doi.org/10.1161/CIRCRESAHA.109.207852>

- Huang J, Yamashiro Y, Papke CL et al (2013) Angiotensin-converting enzyme-induced activation of local angiotensin signaling is required for ascending aortic aneurysms in fibulin-4-deficient mice. *Sci Transl Med*. <https://doi.org/10.1126/scitranslmed.3005025>
- Humphrey JD, Schwartz MA, Tellides G, Milewicz DM (2015) Role of mechanotransduction in vascular biology: focus on thoracic aortic aneurysms and dissections. *Circ Res* 116:1448–1461. <https://doi.org/10.1161/circresaha.114.304936>
- Jondeau G, Boileau C (2012) Genetics of thoracic aortic aneurysms. *Curr Atheroscler Rep* 14:219–226. <https://doi.org/10.1007/s11883-012-0241-4>
- Maas SA, Ellis BJ, Ateshian GA, Weiss JA (2012) FEBio: finite elements for biomechanics. *J Biomech Eng* 134:11005. <https://doi.org/10.1115/1.4005694>
- Marque V, Kieffer P, Gayraud B et al (2001) Aortic wall mechanics and composition in a transgenic mouse model of Marfan syndrome. *Arterioscler Thromb Vasc Biol* 21:1184–1189. <https://doi.org/10.1161/hq0701.092136>
- Martin C, Sun W, Pham T, Elefteriades J (2013) Predictive biomechanical analysis of ascending aortic aneurysm rupture potential. *Acta Biomater* 9:9392–9400. <https://doi.org/10.1016/j.actbio.2013.07.044>
- Masuda Y, Yamada Z, Morooka N et al (1991) Prognosis of patients with medically treated aortic dissections. *Circulation* 84:III7–III13
- Pereira L, Lee SY, Gayraud B et al (1999) Pathogenetic sequence for aneurysm revealed in mice underexpressing fibrillin-1. *Proc Natl Acad Sci USA* 96:3819–3823
- Rateri DL, Davis FM, Balakrishnan A et al (2014) Angiotensin II induces region-specific medial disruption during evolution of ascending aortic aneurysms. *Am J Pathol* 184:2586–2595. <https://doi.org/10.1016/j.ajpath.2014.05.014>
- Rocha KR, Yezzi AJ, Prince JL (2007) A hybrid Eulerian–Lagrangian approach for thickness, correspondence, and gridding of annular tissues. *IEEE Trans Image Process* 16:636–648. <https://doi.org/10.1109/TIP.2007.891072>
- Schwill S, Seppelt P, Grünhagen J et al (2013) The fibrillin-1 hypomorphic mgR/mgR murine model of Marfan syndrome shows severe elastolysis in all segments of the aorta. *J Vasc Surg* 57:1628–1636. <https://doi.org/10.1016/j.jvs.2012.10.007>
- Shahmansouri N, Alreshidan M, Emmott A et al (2016a) Investigation on the regional loss factor and its anisotropy for aortic aneurysms. *Materials (Basel)* 9:1–16. <https://doi.org/10.3390/ma9110867>
- Shahmansouri N, Alreshidan M, Emmott A et al (2016b) Evaluating ascending aortic aneurysm tissue toughness: dependence on collagen and elastin contents. *J Mech Behav Biomed Mater* 64:262–271. <https://doi.org/10.1016/j.jmbbm.2016.08.006>
- Trachet B, Piersigilli A, Fraga-Silva RA et al (2016) Ascending aortic aneurysm in angiotensin II-infused mice: formation, progression, and the role of focal dissections. *Arterioscler Thromb Vasc Biol* 36:673–681. <https://doi.org/10.1161/ATVBAHA.116.307211>
- Tsamis A, Phillippi JA, Koch RG et al (2013) Fiber microarchitecture in the longitudinal-radial and circumferential-radial planes of ascending thoracic aortic aneurysm media. *J Biomech* 46:2787–2794. <https://doi.org/10.1016/j.jbiomech.2013.09.003>
- van der Meer FJ, Faber DJ, Cilesiz I et al (2011) Temperature-dependent optical properties of individual vascular wall components measured by optical coherence tomography. *J Biomed Opt* 11:41120. <https://doi.org/10.1117/1.2333613>
- Wilson JS, Humphrey JD (2014) Evolving anisotropy and degree of elastolytic insult in abdominal aortic aneurysms: potential clinical relevance? *J Biomech* 47:2995–3002. <https://doi.org/10.1016/j.jbiomech.2014.07.003>
- Wu D, Shen YH, Russell L et al (2013) Molecular mechanisms of thoracic aortic dissection. *J Surg Res* 184:907–924. <https://doi.org/10.1016/j.jss.2013.06.007>
- Yezzi AJ, Prince JL (2003) An Eulerian PDE approach for computing tissue thickness. *IEEE Trans Med Imaging* 22:1332–1339. <https://doi.org/10.1109/TMI.2003.817775>

**Publisher's Note** Springer Nature remains neutral with regard to jurisdictional claims in published maps and institutional affiliations